J Mater Sci (2008) 43:3704–3712
DOI 10.1007/s10853-008-2600-7

# Probing the structure of nanograined CuO powders

**Ana E. Bianchi · Tomás S. Plivelic · Graciela Punte · Iris L. Torriani**

Received: 19 September 2007 / Accepted: 17 March 2008 / Published online: 4 April 2008


**Abstract** The microstructural properties of polycrystalline CuO powders and their evolution during controlled high energetic ball milling (HEBM) were studied using conventional X-ray diffraction (XRD) techniques and in situ temperature-dependent small and wide angle scattering (SAXS–WAXS) synchrotron radiation experiments. Volume weighted average grain size, unit cell expansion, oxygen deficiency, and microstrain values as a function of milling time were obtained from XRD. SAXS data revealed different nanostructures for samples synthesized by one-step solid-state reaction (SSR) or HEBM-treated powders. The latter presented the characteristics of a multilayered nanoscale solid system with surface fractal behavior. Correlation of the XRD microstructural parameters and the power law exponent of the SAXS curves as a function of temperature and milling time provided a coherent picture of the structure of HEBM-treated powders. The overall structural information presented in this article may shed some light on the macroscopic physical properties of CuO nanostructures.

A. E. Bianchi · G. Punte
LANADI – Departamento de Física, Facultad de Ciencias Exactas – UNLP, La Plata, Argentina

A. E. Bianchi
e-mail: bianchi@fisica.unlp.edu.ar

G. Punte
e-mail: punte@fisica.unlp.edu.ar

T. S. Plivelic
Laboratorio Nacional de Luz Sincrotron, Campinas, Sao Paulo 13083-970, Brazil

I. L. Torriani (✉)
Instituto de Física, Universidade Estadual de Campinas, Cidade Universitária, Campinas, Sao Paulo 13083-970, Brazil
e-mail: torriani@ifi.unicamp.br

## Introduction

The synthesis of materials and development of devices with new properties by means of the controlled manipulation of their microstructure has become an active interdisciplinary field. In particular, nanostructured materials [1] call the attention of many researchers as they may exhibit a unique set of physicochemical properties, essentially different from those of single crystals or coarse-grained polycrystalline materials [2, 3]. These differences are assumed to come mainly from grain (or crystallite) size effects and from the presence of high densities of grain or phase boundaries, which, when the materials are monophasic, tend to self organize forming three-dimensional networks [4–6]. This led to the investigation of the interface structure and the associated grain boundary network either as an essential step for understanding the macroscopic properties of nanomaterials or to tailor functional ones [7, 8].

Within this scenario, interest in nanoparticles with magnetic properties has increased in the past few years due to their many applications. Antiferromagnetic (AF) systems represent a very interesting subset since the uncompensated exchange coupling of the grain surface spins leads to significant magnetic moment per grain even though the spins in the core are antiferromagnetically ordered [9]. Taking into account the relevance of the latter systems we designed experiments to obtain representative information of the overall microstructure of a well-defined antiferromagnetic nanostructured system. The AF cupric oxide, CuO, was chosen because of its unique bulk properties (e.g. crystal structure [10] and magnetic properties [11, 12]), some of which (like strong antiferromagnetic Cu–O–Cu correlation and static charge order [13, 14]), are similar to those found in High Tc superconductor cuprates.

Despite being a system far simpler than those cuprates, the nature of many properties of CuO is still unclear, making the system to be the subject of renewed attention [11–18].

HEBM has been widely used (in spite of some drawbacks of the method, like possible contamination) to synthesize nanocrystals [19, 20] due to its simplicity, low cost, and applicability to essentially all classes of materials. Solid-state reaction at room temperature (SSR) is another synthesis path usually employed to obtain nanoparticles. It has been found previously that CuO nanostructures produced by high energetic ball milling HEBM or SSR exhibit dissimilar magnetic [21, 22] and electrical conductivity [23]. These properties are also known to be different from those of polycrystalline CuO. Consequently, a thorough investigation of the structural properties using samples obtained by both methods was considered essential to characterize CuO nanosystems.

Conventional X-ray powder diffraction techniques (XRD) can furnish valuable results related to the mean crystalline structure and microstructure of nanograined materials. Nonetheless, when analyzing materials by means of X-rays, colloidal size heterogeneities of the electron density cause X-ray scattering at very low angles [24, 25]. Then, for electron density fluctuations in the range 1–100 nm, small angle X-ray scattering (SAXS) can provide significant information on the scattering entities. Dimensional parameters, nanoscale features and the nature of the interface can also be described in most cases [24–28]. This technique is especially reliable when high intensity X-ray sources are used for the experiments.

XRD and SAXS experiments were aimed at obtaining a detailed microstructural description of the prepared nanocrystalline CuO samples, which could be related to their macroscopic properties. In situ combined SAXS and wide angle (WAXS) experiments were performed at room temperature (RT) and as a function of temperature. The latter were useful to further investigate changes in microstructural parameters calculated from the scattering intensity curves.

## Experiments

HEBM nanocrystalline powders were obtained using CERAC pro analysis cupric oxide powder. The samples, labeled $S_{ij}$ ($i$ = A–B; $j$ = 1–5) were produced by controlled ball milling keeping a fixed powder-to-ball mass ratio ($r$ = 14:3). The copper oxide mass used was 345 mg and 109 mg for samples A and B, respectively. An unsealed cylindrical steel vial with one steel ball in a vertical vibratory mixer mill operating at 50 Hz with 1 cm of amplitude was used in both cases. Different samples within each set were obtained by cycles of half an hour of grinding and 1 h of rest to attain the total milling time, $t_m$, as follows: $S_{i1}$ (60 min), $S_{i2}$ (210 min), $S_{i3}$ (360 min), $S_{i4}$ (540 min), and $S_{i5}$ (720 min). The nanocrystalline sample used as control, labeled SSR, was synthesized by a one-step solid-state reaction at room temperature [20]. Energy dispersive X-ray analyses (EDAX) of the HEBM samples were performed using a JEOL JEM-2000FX microscope operating at 200 keV to check possible contamination from vials or steel balls.

Cu K$\alpha$ radiation ($\lambda$ = 1.5406 Å) was used to obtain XRD data of all the samples at RT, in a standard Phillips PW-1710 diffractometer with a scintillation counter and an exit beam graphite monochromator. Data were collected in the $20° \leq 2\theta \leq 120°$ range, with 0.02° step width and counting time no less than 15 s per step. The Rietveld analysis of the data was carried out using the Fullprof program [29]. SAXS experiments for all the samples were performed at the D11A workstation of the Brazilian Synchrotron Light Source (LNLS), Campinas, Brazil [30]. The powder samples were mounted filling homogeneously a spacer window between very thin (30 μm) mica plates. Samples were prepared with a maximum thickness of 0.1 mm to avoid possible multiple scattering effects.

The exposures were made using a vacuum chamber directly connected to the beam path. The wavelength used was 1.757 Å. For the set of samples $S_A$ the range of the modulus of the momentum vector detected in the experiments was $0.01 \leq q \leq 0.3$ Å$^{-1}$ ($q = (4\pi/\lambda)\sin\theta$, $2\theta$ = scattering angle). For set $S_B$ the range of $q$ values registered was $0.019 \leq q \leq 0.6$ Å$^{-1}$. All measurements were made using a linear position sensitive detector. In situ SAXS and WAXS experiments as a function of sample temperature and annealing time were performed using transmission geometry. For this purpose an especially dedicated high-temperature chamber [31] was used. In order to avoid the influence of the known phase transition at approximately 800 K [13, 14] the measurements were programmed to isochronously cover the range between 298 and 698 K. After that, an isothermal treatment was performed at 698 K. Each WAXS and SAXS spectrum was taken in succession after stabilizing the sample temperature for 5 min. The SAXS $q$ range detected in these experiments was $0.01 \leq q \leq 0.3$ Å$^{-1}$. WAXS measurements were made in the $30° \leq 2\theta \leq 80°$ range using an image plate detector. SAXS data treatment was performed using the program TRAT1D [32], which corrects the intensity values for sample absorption, background contribution and detector response.

## Results

EDAX data showed no contamination of the HEBM samples after the milling process. The existence of

superimposed reflections in the diffraction patterns (shown in Fig. 1a, b) did not allow a single valued peak deconvolution of XRD data. This prevented the use of the more usual approximations to determine the grain size and the existence of microstrain. Consequently, the average volume-weighted crystallite size, $\langle D \rangle_v$, and the weighted average strain, $\langle \tilde{\varepsilon} \rangle$, for RT data were determined from the Rietveld analysis of the diffraction patterns using the Desai and Young model [33]. Modified pseudo-Voigt functions were found to provide the best fit for the line profiles. The initial structural model was the one proposed by Åsbrink and Norrby [10]. Rietveld analysis also yielded the unit cell volume, $V_C$, and the oxygen atom occupation number, $n_O$. The results extracted from the XRD data analysis are shown in Table 1. Figure 2 shows a typical Rietveld fit.

SAXS curves for the HEBM samples did not exhibit, within the low $q$ range, a clear contribution from particle scattering. For the medium range $q$ values, a power law behavior, $I(q) \propto 1/q^{\alpha}$, $(3 < \alpha < 4)$ was observed extending for approximately one decade. In spite of poor statistics, at large $q$ values the intensity decreases as $q^{-4}$ following Porod's law [25]. Representative scattering curves obtained for the ball-milled samples $S_{A1}$, $S_{A3}$, and $S_{A5}$ are shown in Fig. 3. It is interesting to note that the SAXS intensity curve corresponding to the SSR sample showed a small bent at low and intermediate $q$ values, and unlike the other samples, the Porod regime, $\alpha \approx 4$, was rapidly attained (Fig. 4). The values of the power law coefficient for all the samples studied at RT are presented in Table 1.

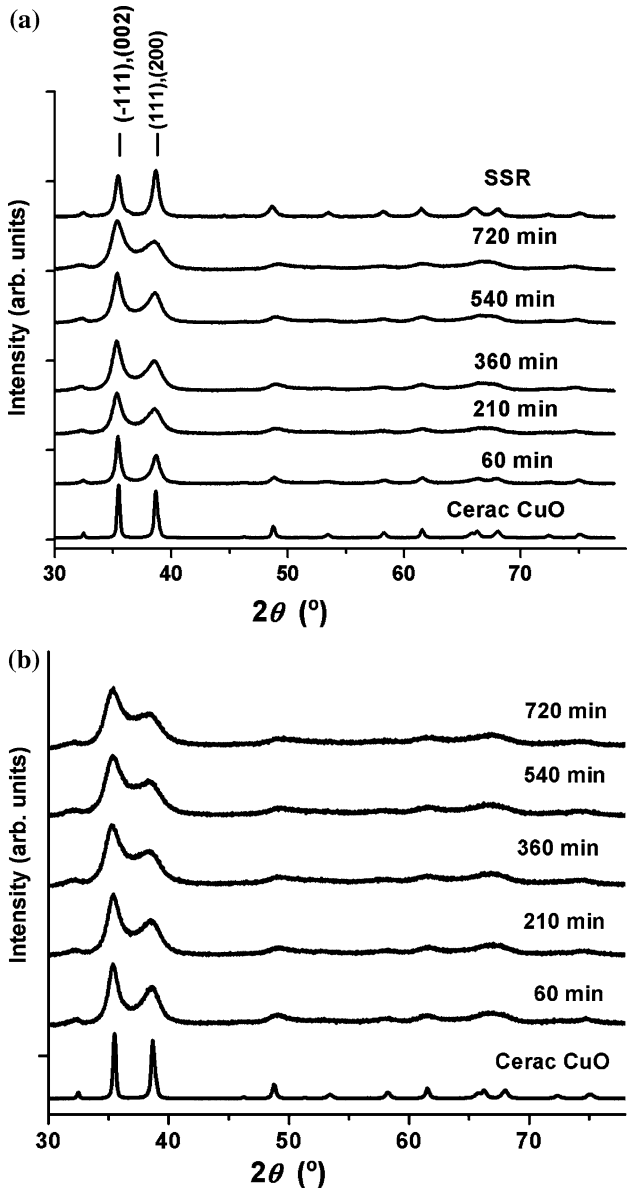


**Fig. 1** (**a**) RT XRD patterns of HEBM CuO, set A (Miller indices for the two superposed lines are indicated). SSR and commercial CuO are also included for comparison; (**b**) RT XRD patterns of HEBM CuO, set B

**Table 1** Microstructural parameters, $\langle D \rangle_v$ and $\langle \tilde{\varepsilon} \rangle$, cell volume, $V_C$, oxygen occupancy, $n_O$ (full = 1.0), and power law exponent ($\alpha$)

| Sample $t_m$ (min) | $\langle D \rangle_v$ (nm) | $\langle \tilde{\varepsilon} \rangle$ | $V_C$ (Å$^3$) | $n_O$ | $\alpha$ |
|---|---|---|---|---|---|
| $S_{A1}$(60) | 35.1(1) | 0.012(1) | 81.214(1) | 0.94(1) | 3.76(1) |
| $S_{A2}$(210) | 30.4(1) | 0.031(1) | 81.454(1) | 0.90(2) | 3.40(1) |
| $S_{A3}$(360) | 24.6(1) | 0.036(1) | 81.830(2) | 0.86(1) | 3.55(1) |
| $S_{A4}$(540) | 21.0(7) | 0.039(1) | 81.899(1) | 0.84(1) | 3.37(1) |
| $S_{A5}$(720) | 21.0(5) | 0.042(1) | 82.620(1) | 0.88(2) | 3.39(1) |
| $S_{B1}$(60) | 16.1(2) | 0.030(1) | 82.105(1) | 0.82(2) | 3.33(1) |
| $S_{B2}$(210) | 12.9(3) | 0.031(1) | 82.302(1) | 0.82(2) | 3.21(1) |
| $S_{B3}$(360) | 10.0(2) | 0.034(1) | 82.584(1) | 0.80(1) | 3.28(1) |
| $S_{B4}$(540) | 9.5(2) | 0.035(1) | 82.702(1) | 0.80(1) | 3.09(1) |
| $S_{B5}$(720) | 9.5(2) | 0.037(1) | 83.166(1) | 0.80(1) | 3.00(1) |
| SSR | 21(1) | 0.0 | 81.319(1) | 1.00 | 3.99(1) |

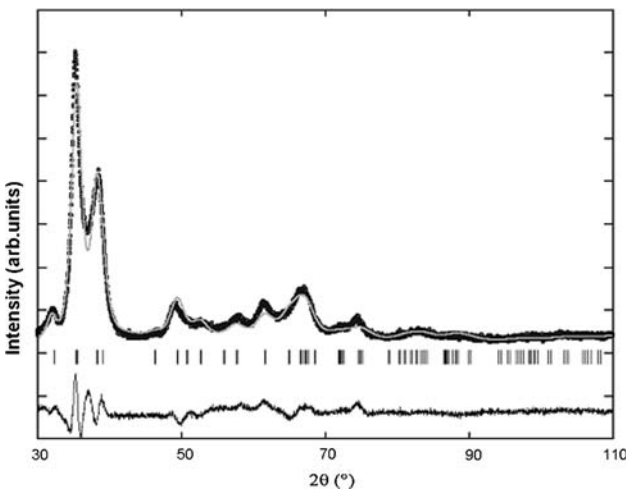


**Fig. 2** $S_{A5}$ experimental and fitted XRD patterns. Vertical bars: CuO line positions. Difference plot shown at the bottom

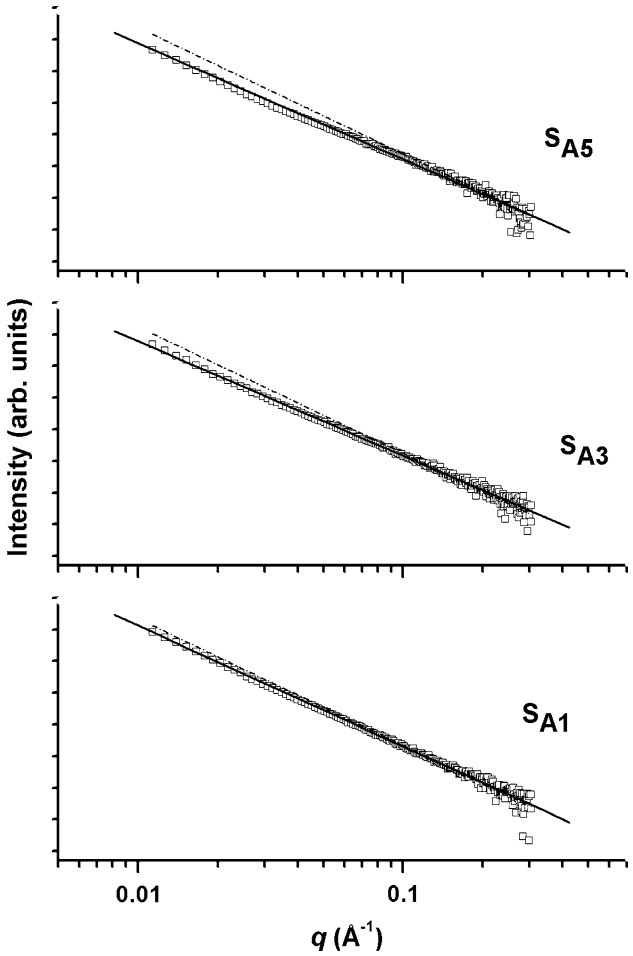


**Fig. 3** SAXS curves for HEBM samples $S_{A1}$, $S_{A3}$, and $S_{A5}$. Open squares: experimental points. Continuous line: power law fitting; dotted line: $I(q) \propto q^{-4}$, Porod's law

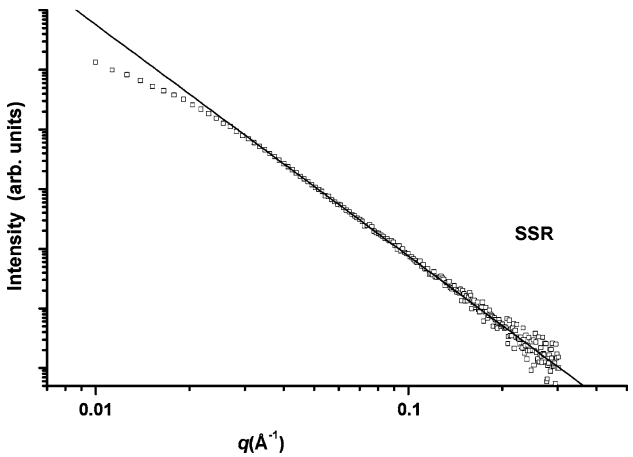


**Fig. 4** SSR sample SAXS curve (open squares). Continuous line: Porod's law

Temperature- and time-dependent in situ WAXS data for the sample $S_{A5}$ are shown in Fig. 5a, b. A reduction in the diffraction line width as a function of the thermal

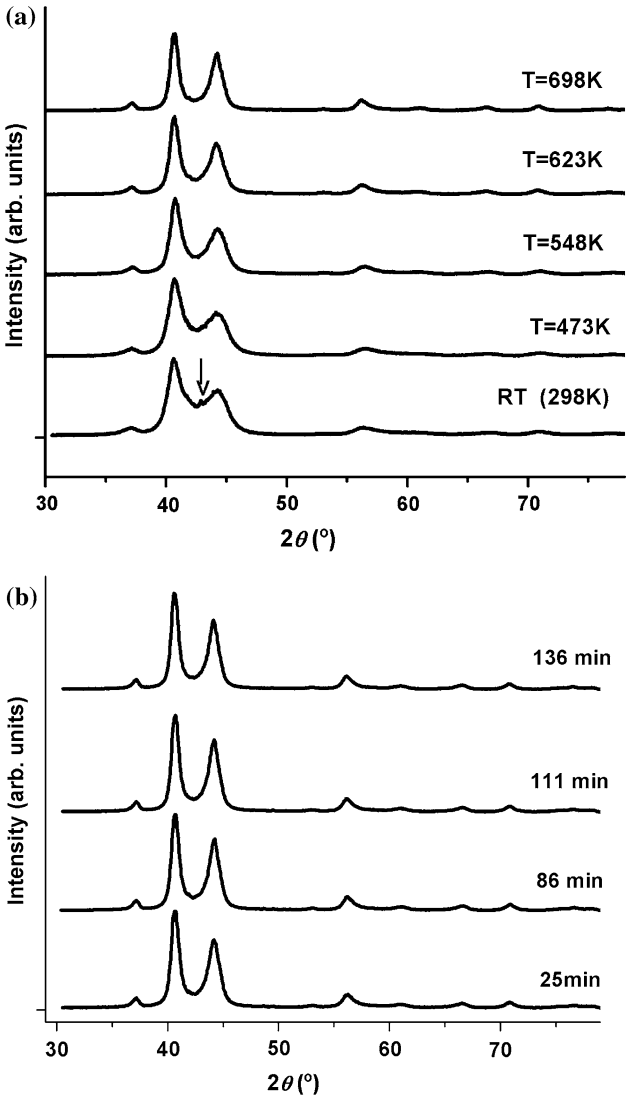


**Fig. 5** $S_{A5}$ WAXS patterns evolution: (**a**) as function of temperature, arrow: mica line from holder; (**b**) as function of time at $T = 698$ K

treatment is observed. The limited range of the wide-angle data provided by the high-temperature chamber did not allow an accurate determination of the crystallographic cell parameters. In spite of that limitation, information on the changes in the average grain size and lattice strain induced by the thermal treatments could be obtained from a Rietveld fitting of line profiles of the collected data.

SAXS spectra obtained for this sample during temperature-dependent experiments are shown in Fig. 6. Only one frame, representative of the 15 frames taken for each temperature, is shown in this figure. Data from isothermal treatment at 698 K were taken at times varying from 7.5 to 118.5 min.

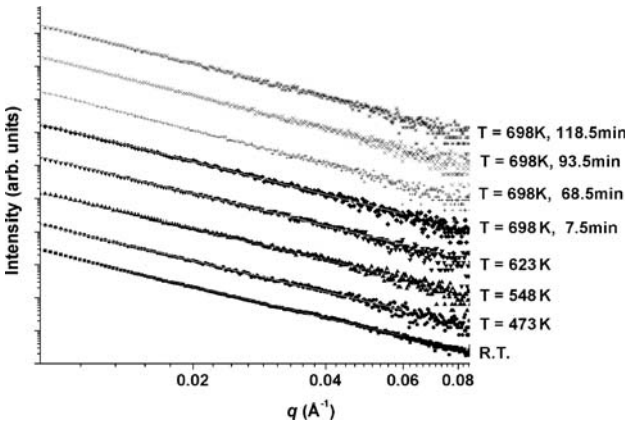


**Fig. 6** $S_{A5}$ SAXS curves as function of thermal treatments; points: experimental data; continuous lines: linear fit

## Discussion

### Parameters obtained from XRD

The results of the Rietveld analysis of XRD data, summarized in Table 1, show a decrease in $\langle D \rangle_v$ with milling time $t_m$. $\langle D \rangle_v$ values go down from the commercial powder grain size of $\approx 1$ μm to 21(1) and 9.5(2) nm, for samples $S_{Aj}$ and $S_{Bj}$, respectively. After 540 min of mechanical treatment $\langle D \rangle_v$ reaches a stable value within experimental errors in both sets of samples. Additional milling time only produces small changes in lattice strain $\langle \tilde{\varepsilon} \rangle$. A concomitant increase of $\langle \tilde{\varepsilon} \rangle$ with $t_m$ is observed. In the $S_{Aj}$ samples the strain value increases steadily with $t_m$, reaching, in $S_{A5}$, approximately 10 times the value found in the coarse commercial powder (CCP), 0.004(1). In the $S_{Bj}$ samples, probably due to the smaller amount of powder treated, the effect of attrition on the $\langle \tilde{\varepsilon} \rangle$ values is very noticeable even at the lowest $t_m$ (60 min), where the strain value reaches a figure seven times the value found in CCP. Further milling induces a relatively smaller strain increment ($\approx 25\%$) and $\langle D \rangle_v$ diminishes by approximately 40%.

In accordance with other authors' observations in CuO and other partially covalent oxides [21, 34, 35], an expansion in the unit cell volume was observed as crystallite size decreased, reaching a maximum of $\approx 2\%$ in the $S_{Aj}$ samples and 3% in the $S_{Bj}$ samples. Studying covalent or partially covalent oxides other authors reported not only lattice expansion, but also a size-driven transformation to a higher-symmetry phase as particle size decreased [36]. Ayyub et al. [37] have also found in a significant number of oxides, which included several high Tc cuprates, a monotonic O content reduction with particle size. However, they concluded that enhancement in oxygen mobility and occupancy drop does not appear to be a direct result of crystallite size reduction. They explained cell expansion as due to cooperativity lessening within covalent chains, which is caused by the reduction of the length scale of the atomic arrangement. None of our samples showed a higher-symmetry phase but, as discussed above, they present lattice expansion. Moreover, a detailed comparison of all the values obtained for $\langle D \rangle_v$, $\langle \tilde{\varepsilon} \rangle$ and $V_C$ listed in Table 1, seems to indicate that $\langle D \rangle_v$ reduction may not be the only factor to induce cell expansion. For instance, examination of the values corresponding to samples $S_{B3}$, $S_{B4}$, and $S_{A5}$ shows that the cell volume for sample $S_{A5}$ lays between the values found for $S_{B3}$ and $S_{B4}$, although its $\langle D \rangle_v$ value is twice the value found for $S_{B3}$ and $S_{B4}$. $S_{A5}$ also presents an average strain 20% higher than those of $S_{B3}$ and $S_{B4}$. We also observed changes in CuO stoichiometry with milling time. Oxygen reduction reaches $\approx 15\%$ in the $S_{Aj}$ samples and $\approx$ 20% in the $S_{Bj}$ samples. These findings strongly suggest that the increase of $V_C$, as a function of $t_m$, not only depends on $\langle D \rangle_v$ drop, but also on the degree of microstrain and on oxygen occupancy. The results coming from the SSR sample reinforce this idea. Rietveld analysis of XRD RT data for this sample yielded a $\langle D \rangle_v$ value similar to that of samples $S_{A4}$ and $S_{A5}$. However, at odds with the HEBM samples discussed above, it presents no average microstrain. Besides, its $V_C$ is only 0.3% higher than the CCP value, 81.250(1) $Å^3$, and no oxygen deficiency could be detected within experimental errors.

Taking into account all the above results we can assume that in the HEBM samples, besides $\langle D \rangle_v$ value reduction, either strain or oxygen depletion within the crystallites might have disrupted the known long-range Cu–O–Cu arrangements present in bulk CuO [11, 12] weakening bonds and helping cell expansion. The influence of strain in cell expansion has been explored by different authors. Nazarov et al. [38] suggested that crystal lattice expansion of ultra fine-grained materials could be due to non-linear effects caused by the existence of a stress field. In the case of materials produced by severe plastic deformation techniques, defects, ensembles of disclinations and long-range stress fields have been proposed as source of macroscopic properties modification.

### Nanostructure morphology revealed by SAXS

The information obtained from diffraction data yields an excellent description of the ordered crystalline phase present in the samples through the parameters $\langle D \rangle_v$, $\langle \tilde{\varepsilon} \rangle$, $V_C$ and $n_O$. It is important, though, to obtain additional information on the CuO system as a whole, in a context that includes the less ordered intergrain nanophase region. Small angle X-ray scattering experiments allow us to study the reciprocal space intensity resulting from electron density inhomogeneities in the samples. If a plausible model can be assumed, subsequent calculations using the

experimental intensity data can lead to the determination of parameters related to the real space nanostructure.

The SAXS curves described in "Results" section do not yield a straightforward and general description of the nature of the samples and different models have to be adopted in each case. The different atomic density between the crystalline and interface components gives rise to an electron density contrast and the samples could adequately be described as a two-phase system having constant average electron density for each component often pictured as crystallites surrounded by ordered (or disordered) intergrain atomic arrangements. A fairly realistic model for the nanosized scatterers should also consider them as polydisperse in shape and size, with possibly non-smooth interface boundaries. In accordance with this structural model, we found that the corrected intensity curve for the SSR sample admits a reasonable fitting if we treat it as a polydisperse system of uniform spherical particles (see Fig. 7). The complete scattering curve can be approximated using the GNOM program [39]. This calculation also renders the average radius of gyration of the scattering particles ($\langle R_g \rangle = 16(1)$ nm), and the volume size distribution function for a polydisperse system, $D_v(r)$ ($r =$ particle radius), shown in the inset of Fig. 7, which presents a maximum centered at approximately 7.7 nm.

A volume-weighted value of the average particle size is calculated using the following equation:

$$\langle R \rangle_v = \frac{\int_{R_{\min}}^{R_{\max}} D_v(r) \cdot r \cdot \mathrm{d}r}{\int_{R_{\min}}^{R_{\max}} D_v(r) \cdot \mathrm{d}r} \quad (1)$$

The resulting value $\langle 2R \rangle_v = 21.6$ nm is coherent with the $\langle D \rangle_v$ value obtained from XRD, 21(1) nm. The high $q$ behavior of the log–log intensity plot is found to follow

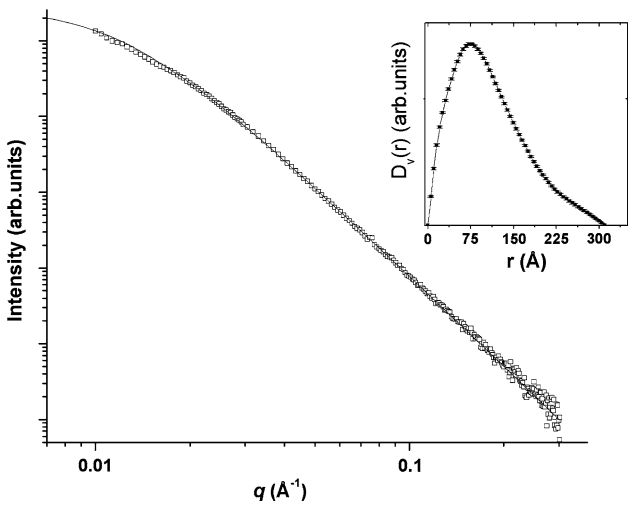


**Fig. 7** SSR SAXS data fit. Continuous line: fitting with GNOM[29] for a polydisperse system of spheres. Volume size distribution function, $D_v(r)$, shown in inset

Porod's law, which would mean that smooth interfaces could be assumed for the system. Given the fact that a fairly clear correlation can be established between the structural size parameters calculated from the XRD data and the information obtained from the analysis of the SAXS curves, this sample was taken as a reference structural model in which the contrast responsible for the X-ray scattering comes from the two-phase system described above.

In the SAXS curves of the HEBM samples shown in Fig. 3a–c, the low $q$ regions do not exhibit the behavior expected for independent particle scattering, and although the curves present a change of slope tending to $\alpha = 4$ for larger $q$ values, no satisfactory GNOM fittings could be made to obtain volume size distribution functions or size parameters. This indicated that these samples could not be described by the same structural model used for the SSR sample and that the only structural information provided by the scattering experiments would be that extracted from the analysis of the power law behavior.

Log $I(q)$ vs. log $q$ plots exhibit power law exponents $\alpha$ varying between 3 and 4 in the $\Delta q$ range 0.02–0.2 $\text{Å}^{-1}$. These values are generally attributed to a surface fractal, for which the scattered intensity follows the law $I(q) \sim 1/q^{\alpha}$ (with $\alpha = 6 - D_s$ and $D_s =$ fractal dimension [28]). The $\alpha$ values corresponding to both sets of HEBM samples, $S_{Aj}$ and $S_{Bj}$, present the same trend, decreasing with the time of mechanical treatment, $t_m$ (see Table 1). It can also be seen that samples produced by the same $t_m$ show $\alpha$ values decreasing when going from set A to set B. This can be correlated with size drop and strain increment induced by the small amount of powder subject to mechanical attrition in set B.

It would be interesting to explain the correlation between the decrease in power law exponent and the cell volume increment (the opposite trend is found when $\langle D \rangle_v$ growth is considered) observed in both series of HEBM samples (Fig. 8a, b).

When trying to describe the nature of the microstructural transformations undergone by the system as a function of $t_m$, a plausible real space model should be used to explain the behavior of the scattering curves for these samples. The formation of nanopowders by severe plastic deformation, like HEBM, originates high density of defects, dislocations, disclinations and grain boundary triple junctions. These, eventually interact, group and clot inducing grain refinement. Rawers and Cook [40], from X-ray diffraction and Mössbauer analysis of iron powders and blends of iron powders, concluded that nanosize grains are not able to sustain dislocations, which rapidly diffuse to the grain boundary region, increasing its disorder and inducing grain lattice expansion and a nanograin interior essentially defect free but affected by strain. There is also evidence of the

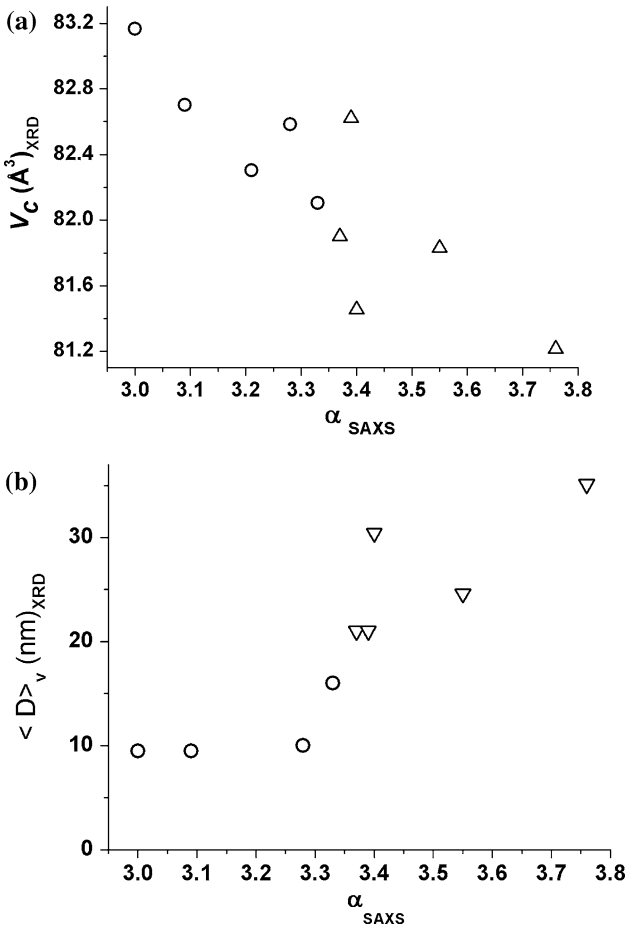


**Fig. 8** Correlation between power law exponent α with: (**a**) the unit cell volume $V_C$; (**b**) the average volume-weighted crystallite size $\langle D \rangle_v$. Open triangles: sample set A; Open circles: sample set B

existence of complex networks (see Ref. [41] and references therein) and self-similarity induced by creep, dislocations and disclinations in several materials [42, 43], including single crystals [44, 45]. These findings are the supporting framework for the description of the ball-milled CuO powders as presenting non-random surface fractal properties. This model, proposed by Schmidt [28], was used by A. Sturm et al. [46] in the description of nanostructured amorphous Si–Au alloys obtained by inner gas condensation and compaction. In our ball-milled samples, the mechanically crushed crystalline grains and grain boundaries, interface defects and eventually closed pores, form a polydisperse system of heterogeneous and deformed solid particles with an average electron density $\rho_p$ corresponding to the mean value of all components. As the process of HEBM proceeds, these particles agglomerate, to form a system of densely packed material and interconnecting channels, resembling a nanoscale multilayered solid with surface fractal behavior [47–50]. The variation of the surface fractal dimension $D_s$ as a function of milling time can, then, be the consequence of the microstructure modifications induced by HEBM.

This microstructural description is consistent with both SAXS and XRD data, since an increment in $t_m$ induces unit cell expansion, a decrease in average grain size and increased lattice strain. Even the oxygen content reduction within the nanocrystals as a function of $t_m$ can be explained as a by-product of the energy transferred to the system by HEBM. This process may locally increase temperature, helping oxygen atoms mobility towards grain boundaries, where they can be trapped within defects.

## In situ SAXS/WAXS experiments

Thermal treatment of HEBM samples is expected to result in strain release and eventual grain growth. In order to find out if thermal treatment also affected the power law exponent α, in situ SAXS and WAXS experiments as a function of temperature and annealing time were performed. From this data, microstrain grain size, and α exponent evolution were obtained. Possible oxygen content variation as thermal treatment proceeded was also quantified. This information allowed to establish plain correlations between the surface fractal properties and microstructure parameters. The sample used for these measurements, $S_{A5}$, was chosen because it had reached, through HEBM, the same crystallite size as the SSR reference sample, except for a larger strain value and lower oxygen content. Furthermore, the power law exponent of the $S_{A5}$ sample had the lowest α value found in the $S_{Aj}$ set of samples.

Figures 9 and 10 show the microstructural parameters and α values evolution as a function of temperature during the isochronous thermal treatment (RT (298 K) $\leq T \leq$ 698 K) and as function of time during the isothermal treatment at 698 K. The analysis of those figures shows that the isochronous thermal treatment induced an increase in both $\langle D \rangle_v$ and the α exponent, together with a decrease in $\langle \tilde{\varepsilon} \rangle$. On the other hand, no significant changes in $\langle D \rangle_v$ seemed to be induced by isothermal treatment, but increase in α and decrease in $\langle \tilde{\varepsilon} \rangle$ are observed. After 86 min of isothermal treatment all these parameters tended to stabilize. A slight increase in α upon annealing (equivalent to a small decrease in $D_s$ from 2.69 to 2.60) can be observed in Fig. 10b. This would indicate that the coarsening of the fractal interfaces due to annealing might be mainly associated not with a change in the fractal dimension but with an increase of the lower cut-off of the surface fractal [50, 51]. Unfortunately, the limited range of our X-ray scattering data is insufficient to allow a more detailed analysis of the effects of annealing at 698 K.

XRD data collected during the thermal treatments did not have the sufficient angular range and were not accurate

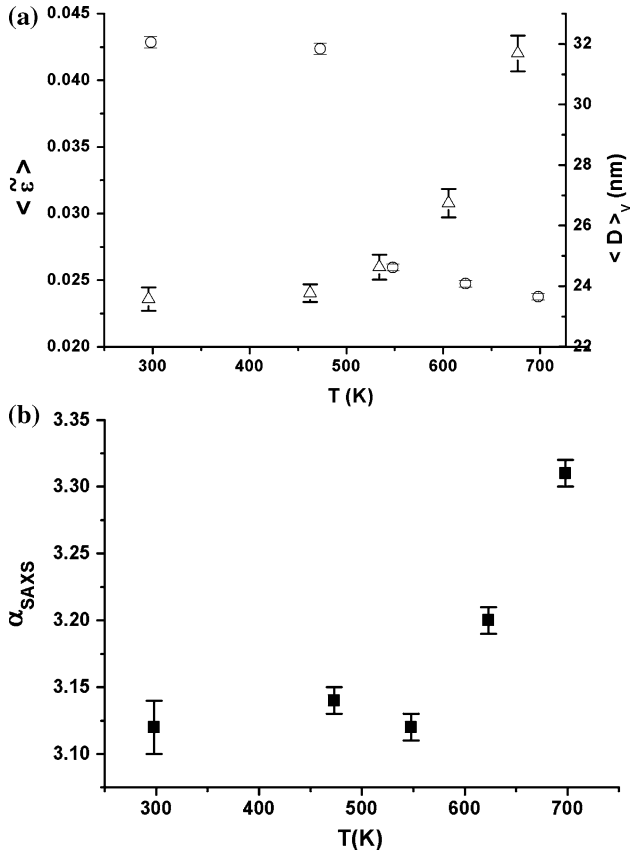


**Fig. 9** Evolution as function of temperature, $298 \leq T \leq 698$ K, of: (**a**) Microstructural parameters, open circles: $\langle\tilde{\varepsilon}\rangle$, open triangles: $\langle D\rangle_v$; (**b**). Power law exponent $\alpha$

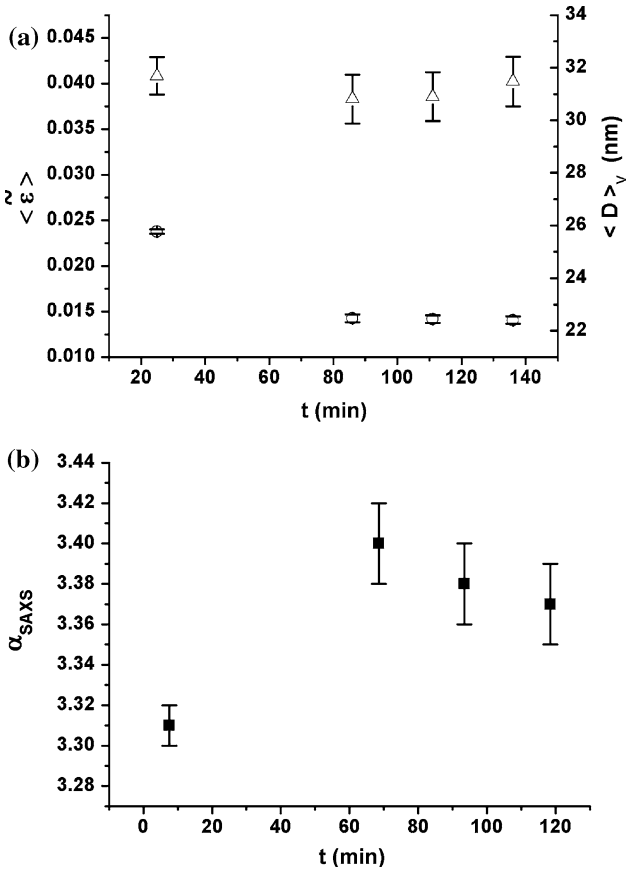


**Fig. 10** Evolution as function of time at $T = 698$ K, of (**a**) Microstructural parameters, Open circles: $\langle\tilde{\varepsilon}\rangle$, open triangles: $\langle D\rangle_v$ and (**b**) power law exponent $\alpha$

enough so as to provide reliable values of $V_C$ or of the oxygen atoms occupation number, $n_O$. However, taking into account that a single CuO phase was detected after the thermal treatment in spite of the sample being in vacuum, we could safely assume that oxygen atoms (trapped at the interface) were reincorporated into the nanocrystals. If oxygen atoms were not available, nanocrystals should have undergone a phase transition to $Cu_2O$. This would lead to the assumption that oxygen atoms, which migrated to the grain boundaries during HEBM, remained concentrated at the interface and were released upon fractal surface modification. This model is consistent with the absence of diffusion through a fractal interface proposed by Maksimenko and Andreev [52]. Regarding the correlation between microstructure and surface fractality, the results shown in Fig. 10 would indicate that a correlation can be established between surface fractal dimension values and strain, though the influence of the oxygen stoichiometry can not be completely disregarded.

The analysis of all the above results show that not only unit cell expansion, microstrain and non-stoichiometry but also interface nature are distinctive of nanograined CuO powders obtained by HEBM, and differentiate these samples from the reference SSR sample. These differences may well explain the disparity in the observed macroscopic properties of SSR and HEBM nanostructured CuO samples with equal average volume-weighted crystallite size described in the literature [21–23].

## Conclusions

XRD and SAXS–WAXS experiments performed as a function of temperature and annealing time on CuO nanostructures obtained by controlled high energetic ball milling and solid-state reaction allowed us to correlate changes in the macroscopic properties with differences in the microstructure parameters induced by the preparation procedure. Besides, in the samples prepared by ball milling a correlation between the changes in the volume weighted average nanocrystals size, the degree of microstrain and the SAXS power law exponent (or surface fractal dimension) with milling time was established. This correlation is consistent with samples being described as polydisperse particle systems made up of strained and non-stoichiometric nanocrystals exhibiting defects and voids and

presenting surface fractal properties. The changes detected in the surface fractal dimension as a function of the milling time and/or thermal treatments may be relevant (or employed) for tailoring macroscopic properties of CuO nanostructures.

**Acknowledgements** The authors thank E. Cabanillas for providing EDAX data and S.J. Stewart for SSR sample supply and helpful discussions. This work was supported by Capes-SeTCIP, CNPq, LNLS, CLAF, CONICET, and UNLP. G.P. is member of CONICET. A.E. Bianchi acknowledges a CAPES grant and a UNLP research fellowship.

## References

1. Gleiter H (2000) Acta Mater 48:1. doi:10.1016/S1359-6454(99)00285-2
2. Lang XY, Zheng WT, Jiang Q (2006) Phys Rev B 73:224444. doi:10.1103/PhysRevB.73.224444
3. Nobis T, Kaidashev EM, Rahm A, Lorenz M, Grundmann M (2004) Phys Rev Lett 93:103903. doi:10.1103/PhysRevLett.93.103903
4. Wang N, Palumbo G, Wang ZR, Erb U, Aust KT (1993) Scripta Metall Mater 28:253. doi:10.1016/0956-716X(93)90572-A
5. Romanov AE (2004) In: Zehetbauer M, Valiev RZ (eds) Nanomaterials by severe plastic deformation. Wiley–VCH Verlag, GmbH & Co, p 213
6. Gomez-Garcia D, Devincre B, Kubin LP (2006) Phys Rev Lett 96:125503. doi:10.1103/PhysRevLett.96.125503
7. Rybchenko SI, Fujishiro Y, Takagi H, Awano M (2005) Phys Rev B 72:054424. doi:10.1103/PhysRevB.72.054424
8. Brahma P, Dutta S, Pal M, Chakravorty D (2006) J Appl Phys 100:044302. doi:10.1063/1.2227669
9. Skumryev V, Stoyanov S, Zhang Y, Hadjipanayis G, Givord D, Nogués J (2003) Nature 423:850. doi:10.1038/nature01687
10. Åsbrink S, Norrby LJ (1970) Acta Crystallogr, Sect B: Struct Crystallogr Cryst Chem 26:8. doi:10.1107/S0567740870001838
11. Koo HJ, Whangbo MH (2003) Inorg Chem 42:1187. doi:10.1021/ic020576k
12. Yamada H, Zheng XG, Soejima Y, Kawaminami M (2004) Phys Rev B 69:104104. doi:10.1103/PhysRevB.69.104104
13. Zheng XG, Xu CN, Tomokiyo Y, Tanaka E, Yamada H, Soejima Y (2000) Phys Rev Lett 85:5170. doi:10.1103/PhysRevLett.85.5170
14. Zheng XG, Yamada H, Scanderbeg DJ, Maple MB, Xu CN (2003) Phys Rev B 67:214516. doi:10.1103/PhysRevB.67.214516
15. Zhang J, Liu J, Peng Q, Wang X, Li Y (2006) Chem Mater 18:867. doi:10.1021/cm052256f
16. Liu Y, Liao L, Li J, Pan C (2007) J Phys Chem C 111:5050. doi:10.1021/jp069043d
17. Filippetti A, Fiorentini V (2005) Phys Rev Lett 95:086405. doi:10.1103/PhysRevLett.95.086405
18. Wu D, Zhang Q, Tao M (2006) Phys Rev B 73:235206. doi:10.1103/PhysRevB.73.235206
19. Koch CC (1993) Nanostruct Mater 2:109. doi:10.1016/0965-9773(93)90016-5
20. Suryanarayana C (2001) Prog Mater Sci 46:1. doi:10.1016/S0079-6425(99)00010-9
21. Borzi RA, Stewart SJ, Mercader RC, Punte G, García FJ (2001) J Magn Magn Mater 226:1513. doi:10.1016/S0304-8853(00)00943-4
22. Stewart SJ, Multigner M, Marco JF, Berry JF, Hernando A, González JM (2004) Solid State Comm 130:247. doi:10.1016/j.ssc.2004.01.032
23. Junciel LD (2003) MSc Thesis. Universidad Nacional de La Plata, La Plata
24. Guinier A, Fournet G (1955) Small angle scattering of X-rays. Wiley, New York
25. Glatter O, Kratky O (1982) Small-angle X-ray scattering. Academic Press, New York
26. Debye P, Bueche AM (1949) J Appl Phys 20:518. doi:10.1063/1.1698419
27. Debye P, Anderson HR Jr, Brumberger H (1957) J Appl Phys 28:679. doi:10.1063/1.1722830
28. Schmidt PW (1991) J Appl Cryst 24:414. doi:10.1107/S0021889891003400
29. Rodriguez-Carvajal J, Fernandez-Diaz MT, Martinez JL (1991) J Phys: Condens Matter 3:3215. doi:10.1088/0953-8984/3/19/002
30. Kellermann G, Vicentin F, Tamura E, Rocha M, Tolentino H, Barbosa A, Craievich A, Torriani I (1997) J Appl Cryst 30:880. doi:10.1107/S0021889897001829
31. Kellermann G, Craievich AF, Newenschwander R, Plivelic TS (2003) Nucl Instr Meth B 199:112. doi:10.1016/S0168-583X(02)01422-2
32. Oliveira CLP (2003) TRAT1D—Computer program for SAXS data treatment. LNLS technical manual MT 01/2003, Campinas
33. Young RA (1993) The Rietveld method. Oxford University Press
34. Zhang F, Chan SW, Spanier JE, Apak E, Jin Q, Robinson RD, Herman IP (2002) Appl Phys Lett 80:127
35. Li G, Boerio-Goates J, Woodfield BF, Li L (2004) Appl Phys Lett 85:2059
36. Palkar VR, Ayyub P, Chattopadhyay S, Multan M (1996) Phys Rev B 53:2167. doi:10.1103/PhysRevB.53.2167
37. Ayyub P, Palkar VR, Chattopadhyay S, Multan M (1995) Phys Rev B 51:6135. doi:10.1103/PhysRevB.51.6135
38. Nazarov AA, Romanov AE, Valiev RZ (1993) Acta Metall Mater 41:1033. doi:10.1016/0956-7151(93)90152-I
39. Semenyuk AV, Svergun DI (1991) J Appl Cryst 24:485. doi:10.1107/S0021889891001280
40. Rawers J, Cook D (1999) Nanostruct Mater 11:331. doi:10.1016/S0965-9773(99)00049-5
41. Minich RW, Schuh CA, Kumar M (2002) Phys Rev B 66:52101. doi:10.1103/PhysRevB.66.052101
42. Tanaka M, Kayama A, Ito Y, Kato R (1998) J Mater Sci 33:3351. doi:10.1023/A:1013241531412
43. Hisatsune K, Takuma Y, Tanaka Y, Udo K, Kawasaki K (1998) J Mater Sci 33:4783. doi:10.1023/A:1004409725726
44. Groma I, Bakó B (2000) Phys Rev Lett 84:1487. doi:10.1103/PhysRevLett.84.1487
45. Székely F, Groma I, Lendvai J (2000) Phys Rev B 62:3093. doi:10.1103/PhysRevB.62.3093
46. Sturm A, Wiedenmann A, Wollenberger H (1995) Mater Sci Eng B 32:295. doi:10.1016/0921-5107(95)03020-4
47. Tanaka M (1995) J Mater Sci 30:3668. doi:10.1007/BF00351883
48. Tanaka M (1996) J Mater Sci 31:749. doi:10.1007/BF00367895
49. Lebedev V, Didenko V, Lapin A, Konoplev K, Orlova D, Török G, Rétfalvi E (2003) J Appl Cryst 36:629. doi:10.1107/S0021889803003996
50. Streitenberger P, Föster D, Kolbe G, Veit P (1996) Script Mater 34:111. doi:10.1016/1359-6462(95)00477-7
51. Streitenberger P (2000) In: Novak MM (ed) Paradigms of complexity—fractals and structures in the sciences. World Scientific, Singapore, p 135
52. Maksimenko VV, Andreev GB (2001) Physica A 300:339. doi:10.1016/S0378-4371(01)00326-0